Acta Geotechnica (2017) 12:1193–1205
DOI 10.1007/s11440-017-0576-7

RESEARCH PAPER

Quantifying the heterogeneity of shale through statistical combination of imaging across scales

Shabnam J. Semnani[1] · Ronaldo I. Borja[1]

Received: 17 December 2016 / Accepted: 20 July 2017 / Published online: 22 August 2017

Abstract Shale is a highly heterogeneous material across multiple scales. A typical shale consists of nanometer-scale pores and minerals mixed with macroscale fractures and particles of varying size. High-resolution imaging is crucial for characterizing the composition and microstructure of this rock. However, it is generally not feasible to image a large sample of shale at a high resolution over a large field of view (FOV), thus limiting a full characterization of the microstructure of this material. We present a stochastic framework based on multiple-point statistics that uses high-resolution training images to enhance low-resolution images obtained over a large FOV. We demonstrate the approach using X-ray micro-tomography images of organic-rich Woodford shale obtained at two different resolutions and FOV. Results show that the proposed technique can generate realistic high-resolution images of the microstructure of shale over a large FOV.

Keywords Multi-scale imaging · Multiple point statistics · Porous media · Shale · Stochastic simulation · X-ray micro-CT

1 Introduction

Shale is a highly heterogeneous rock at multiple scales. A typical shale consists of nanometer-scale pores within organic matter, nanometer- to micron-sized inorganic pores, and micron- to millimeter-sized fractures and particles [1, 2, 4, 43, 59, 61]. Imaging and visualization of the microstructure of a shale are essential steps toward characterizing the heterogeneity of this material. High-resolution imaging has been conducted by a number of authors using a variety of techniques such as X-ray computed tomography (CT) [6, 32, 37], X-ray micro-tomography (micro-CT) [9, 21, 29, 32, 55, 62, 66], transmission X-ray microscopy (TXM) [58], and focused ion beam/scanning electron microscopy (FIB/SEM) [10, 19, 29]. Advances in high-resolution imaging capabilities such as SEM, TXM [44], and X-ray nano-tomography [23] have made it possible to image heterogeneous materials down to the nanoscale resolution. However, when it comes to the state-of-the-art imaging capabilities, there is an inherent conflict between resolution and field of view (FOV): Higher resolution comes with a more limited FOV, whereas larger FOV is obtained at the expense of resolution. In particular, X-ray tomography techniques require a smaller sample size to achieve a higher resolution. Consequently, multiscale imaging, which entails joint application of imaging techniques with different resolutions and FOV, is often employed. Two critical questions then naturally follow: First, how can information obtained at different scales be combined to fully characterize a heterogeneous material? Second, how representative are the high-resolution images captured over a small area in 2D and over a small volume in 3D? The present work intends to provide a statistical approach toward answering these questions.

Multiscale imaging has been a subject of growing importance, especially in the field of geosciences [18], due to the significance of material heterogeneity on every aspect of the material response. In recent years, many researchers have applied imaging techniques with different resolutions and FOV to explore the structure of

✉ Ronaldo I. Borja
borja@stanford.edu

[1] Department of Civil and Environmental Engineering, Stanford University, Stanford, CA 94305, USA

heterogeneous geomaterials [7, 20, 25–27, 29, 33, 34, 36, 51, 60]. A majority of these works consist of obtaining a low-resolution image of a large sample scanned over a large FOV and then selecting regions of interest for further high-resolution imaging. Some of these works have also included registration and fusion of high-resolution images into the low-resolution dataset. In practice, however, high-resolution imaging is only feasible over a small portion of a low-resolution, large-FOV image. To circumvent this limitation, statistical methods are often employed.

Statistical methods have been used widely in the literature to generate random realizations of the microstructure of porous materials such as rocks, with a main focus on generating only the pore space. Among these statistical methods are Markov chain models [63], simulated annealing [17, 40], two-point statistics [5], and multiple-point statistics [47]. Traditionally, two-point statistics and variogram-based methods were used [50], which aim at obtaining a model such that two-point statistical relations in the reconstructed field match with the observed field. These methods are often inadequate for complex structures since they cannot capture connectivity patterns. In recent years, multiple-point statistics (MPS) has received considerable attention. This technique takes into account higher-order statistics, thus allowing for reproduction of complex geological patterns [30]. MPS algorithms such as single normal equation simulation (SNESIM) [54], direct sampling (DS) [41], and image quilting (IQ) [22], pivot around selection of training image(s) and taking the statistics from training images which feature the representative patterns that are subject to simulation. SNESIM has been used widely in the literature for 3D generation of pore space in porous media using 2D [47, 65] or 3D training images [64].

In this paper, we demonstrate a framework based on MPS for enhancing low-resolution image data by including features not captured within the resolution limit. The present framework is based on direct sampling (DS) method [41], which allows us to work with continuous variables and conduct fine-scale simulations conditioned on a coarse-scale dataset [31] to ensure consistency between the two scales of interest. We show how the present framework can be applied for low- and high-resolution X-ray micro-tomography imaging of shale. The presented framework results in high-resolution images over larger FOV, thus facilitating an understanding of the heterogeneity of a shale across scales. Results can be used in a variety of applications, including obtaining the permeability, porosity, and mechanical properties of a shale sample. Apart from the enhanced images, the present approach can also be used to generate realistic digital cores of rocks for the purpose of numerical simulation incorporating microstructural effects on the bulk properties and behavior of a material [11, 12, 13, 49, 56, 57]. Since the present approach is stochastic in nature, multiple realizations of the same domain can also be conducted for uncertainty quantification [24].

2 Statistical approach

When it comes to imaging, there is an inherent conflict between resolution and FOV: The higher the resolution, the more limited the FOV. To illustrate this point, Fig. 1a shows a 2D slice of Woodford shale obtained using X-ray micro-tomography with a pixel resolution of 4.14 μm. Maximum instrument FOV for this scan is about 4 mm. Figure 1b shows a magnified region revealing limited resolution. In contrast, Fig. 1c shows the result of a high-resolution scan of the same region as Fig. 1b, with pixel size of 0.517 μm and a maximum FOV of about 0.5 mm. The grayscale images are based on X-ray attenuation coefficients, with brighter regions corresponding to material of higher density and darker regions corresponding to material of lower density. Two regions marked as “3” in Fig. 1b, c are shown in Fig. 1d, e, respectively. Figure 1e is a zoom of region “3” in Fig. 1c and reveals that the blurred bright region consists of pyrite framboids and organic/pores. Figure 1f shows an enlarged particle from a region marked as “4” in Fig. 1c, which appears to be a pyrite framboid. A comparable region of similar size is shown in Fig. 1g, which shows submicron pyrite particles and organic/pores. Figure 1g is a 2D slice of a subsample with a diameter of about 20 μm and was obtained using TXM at Stanford Synchrotron Radiation Lightsource (SSRL). The image has a resolution of about 30 nm and maximum FOV of 30 μm. The ideal condition would be to have the FOV delineated in Fig. 1a and the resolution of Fig. 1g, but in general this is not feasible.

The stochastic approach presented here is based on the hypothesis that imaging with a lower resolution over larger FOV not only captures large-scale features but also provides information on features below the resolution limit. This is consistent with the knowledge that each voxel in a grayscale image obtained via X-ray tomography is proportional to the average of X-ray attenuation coefficients of the material phases located at that voxel, generally known as partial volume effect [18]. Statistical simulations of fine-scale features therefore need to be consistent with the large-scale information. Consider Fig. 1 as an example. The large bright region marked “1” in Fig. 1b shows that the large pyrite mineral is captured in the low-resolution image, as evidenced by the same region marked on the corresponding high-resolution image in Fig. 1c. On the other hand, the combination of pores, organics, and light mineral particles observed in a nearby region marked “2”

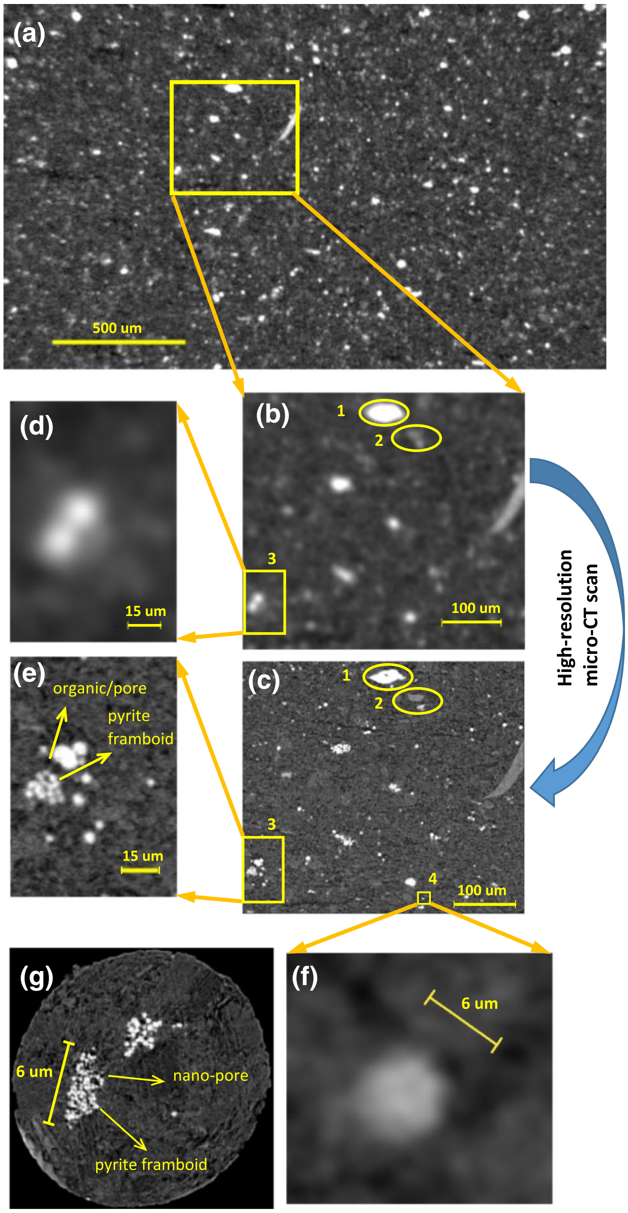

Fig. 1 Multiscale imaging of shale. A single slice of shale with pixel size of 4.14 µm, obtained using a low-resolution micro-tomography scan, is shown in (**a**), and the *marked region* is enlarged in (**b**). **c** Illustrates the same region shown in (**b**) obtained using a micro-tomography scan with a pixel size of 0.517 µm. Region 3 marked in (**b**, **c**) is enlarged in (**d**, **e**), respectively, showing small pyrite particles, framboids, pores/organics, and matrix of low-density minerals and clay which appear as a blurred range of gray values in the low-resolution image. Region 4 marked in (**c**) is enlarged in (**f**) which appears to be a pyrite framboid. A 6-µm-sized framboid comparable to (**f**), shown in (**g**), was obtained using TXM with a resolution of 30 nm

of the same size in Fig. 1c are not resolved in the low-resolution image. Nevertheless, the intensities and distributions of the gray values observed in region "2" marked on Fig. 1b provide some information regarding the phases located in this region.

Based on the aforementioned idea, we demonstrate the application of MPS to generate high-resolution images of fields for which only low-resolution data are available. For this purpose, a high-resolution image and its corresponding low-resolution image form a two-variate training image (TI), which is considered to contain various types of patterns expected to occur in the simulation domain (see Fig. 2). The simulation procedure for the present problem is described here briefly. For further details on the DS algorithm, the reader is referred to [41].

Figure 2a, b schematically shows the fine-scale simulation grid and the corresponding low-resolution image, respectively. The low-resolution image has to be presented in the fine-scale grid system, as shown in Fig. 2c. Figure 2d, e illustrates the high-resolution training image and its corresponding low-resolution image, respectively. The

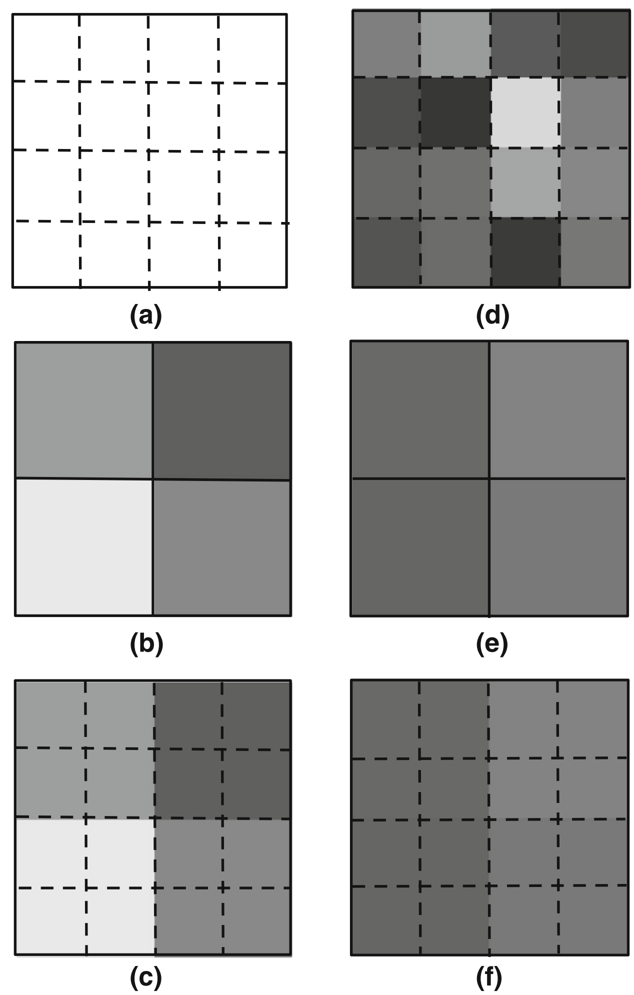

Fig. 2 Schematic of training image and simulation grid. **a** Fine-scale simulation grid. **b** Low-resolution image corresponding to the simulation grid. **c** The same low-resolution image as (**b**) presented in the fine-scale simulation grid system. **d** High-resolution training image. **e** Low-resolution training image. **f** Low-resolution training image presented in the same high-resolution grid as (**d**)

two images are registered and transformed to the same fine-scale grid, as shown in Fig. 2f. In a mathematical setting, our goal is to simulate a random function $Z_h(\boldsymbol{x})$ representing gray-value of a pixel located at position $\boldsymbol{x}$ in the fine-scale simulation grid. The TI is a two-variate field consisting of variables $Z_h(\boldsymbol{y})$ and $Z_l(\boldsymbol{y})$, which correspond to high-resolution and low-resolution images, respectively, where $\boldsymbol{y}$ denotes position vector of each fine-scale pixel in the TI. The conditional cumulative density function for variable $Z_h(\boldsymbol{x})$ can be written as follows:

$$F_h\left(z, \boldsymbol{x}, \boldsymbol{d}_x^h, \boldsymbol{d}_x^l\right) = P\left[Z_h(\boldsymbol{x}) \leq z \mid \boldsymbol{d}_x^h, \boldsymbol{d}_x^l\right] \tag{1}$$

in which

$$\boldsymbol{d}_x^h = \left[Z_h\left(\boldsymbol{x} + \boldsymbol{h}_1^h\right), \ldots, Z_h\left(\boldsymbol{x} + \boldsymbol{h}_{n_h}^h\right)\right] \tag{2}$$

defines a vector containing n_h closest high-resolution pixels to $\boldsymbol{x}$ that are already simulated, and $\boldsymbol{h}_j^h$ is a lag vector from $\boldsymbol{x}$ to neighboring pixels. Similarly,

$$\boldsymbol{d}_x^l = \left[Z_l\left(\boldsymbol{x} + \boldsymbol{h}_1^l\right), \ldots, Z_l\left(\boldsymbol{x} + \boldsymbol{h}_{n_l}^l\right)\right] \tag{3}$$

defines a vector containing n_l closest fine pixels in the low-resolution image of the simulation grid. Some MPS algorithms such as SNESIM [54] for categorical variables scan the TI to build the probability distribution function corresponding to Eq. (1) and sample from that distribution. DS method, on the other hand, relies on a different sampling strategy [41]. The idea is to find a pixel in the TI with neighbors [as defined through lag vectors in Eqs. (2) and (3)] that are similar to neighbors in the simulation grid, and assign the value of that pixel to the simulation grid.

The simulation proceeds by randomly visiting each pixel in the fine-scale simulation grid. For simulating each high-resolution pixel, the lag vectors $\boldsymbol{h}_m^h$ ($m = 1, \ldots, n_h$) and $\boldsymbol{h}_k^l$ ($k = 1, \ldots, n_l$), and the data events $\boldsymbol{d}_x^h$ and $\boldsymbol{d}_x^l$ in the simulation grid are first identified. Subsequently, fine pixels in the TI are visited randomly, and data events $\boldsymbol{d}_y^h$ and $\boldsymbol{d}_y^l$ are obtained from the TI using the same lag vectors $\boldsymbol{h}_m^h$ and $\boldsymbol{h}_k^l$. The similarity between data event observed in the simulation grid and TI is measured by calculating the following distance, and then checking to see if it is smaller than a specified threshold t:

$$d = w_h f\left(\boldsymbol{d}_x^h, \boldsymbol{d}_y^h\right) + w_l f\left(\boldsymbol{d}_x^l, \boldsymbol{d}_y^l\right) < t \tag{4}$$

where w_h and w_l, which satisfy the condition $w_h + w_l = 1$, determine how much weight is assigned to the previously simulated high-resolution data and the given low-resolution data, respectively. $f(\cdot)$ is a function that determines the distance between the two vectors, e.g., the normalized Euclidean distance and Manhattan distance (see [41]). Once a distance $d < t$ is observed, the value of the pixel in the TI is assigned to the simulation grid. If the threshold is not satisfied after scanning a predefined portion of the TI, F, the pixel value corresponding to the smallest d is selected.

3 X-ray micro-tomography imaging

In the present work, a millimeter-sized sample of organic-rich Woodford shale was used. This is the same shale sample studied in [10], obtained from an exploratory wellbore of the northern flank of the Arbuckle uplift, near the Arkoma basin, Pontotoc County, Oklahoma, USA. The corresponding laboratory and field characterization results can be found in [3]. X-ray computed micro-tomography (micro-CT) was performed at Stanford Nano Shared Facilities (SNSF), using Xradia Zeiss 520 Versa. The instrument has a sealed transmission X-ray source with voltage range of 30–160 kV and maximum output of 10 W. The best spatial resolution of the instrument is 0.7 µm, and the minimum achievable pixel size is 70 nm.

First, a low-resolution scan was conducted on the millimeter-sized sample, with the following scan parameters: X-ray source voltage: 40 kV; X-ray source power: 3 W; optical magnification: 4X; source filter: LE2; camera binning: 2; pixel size: 4.14 µm; FOV: 1013 × 1013 pixels. Exposure time was selected as 1 s per projection. 1600 projections were acquired over a 360° rotation, corresponding to an angular increment of 0.225°. The source to rotation axis distance and the detector to rotation axis distance were set to 10.670 and 6.653 µm, respectively. Secondary references with LE6 filter were acquired and applied to reduce possible beam hardening ring artifacts.

Subsequently, without removing the sample from the holder, a high-resolution interior tomography was conducted on a small portion of the sample. The following settings were used for this scan: X-ray source voltage: 60 kV; X-ray source power: 5 W; optical magnification: 40X; source filter: LE3; camera binning: 2; pixel size: 0.517 µm; FOV: 973 × 973 pixels. The source to rotation axis distance and the detector to rotation axis distance were set to 10.963 and 3.812 µm, respectively. To increase the signal-to-noise ratio for this high-resolution interior tomography, the X-ray exposure time has to be much larger than the low-resolution full-FOV scan. Exposure time of 21 s was used in this scan as it provided sufficient signal-to-noise ratio. Moreover, significantly smaller angular increments are required. In this case, 3000 projections over 180° plus the fan angle, corresponding to an angular increment of 0.06° , were found to be sufficient.

Figure 3a shows the low-resolution full-FOV 3D volume imaged with 4.14 µm pixel size. Figure 3b shows the high-resolution 3D volume with 0.517 µm pixel size inside

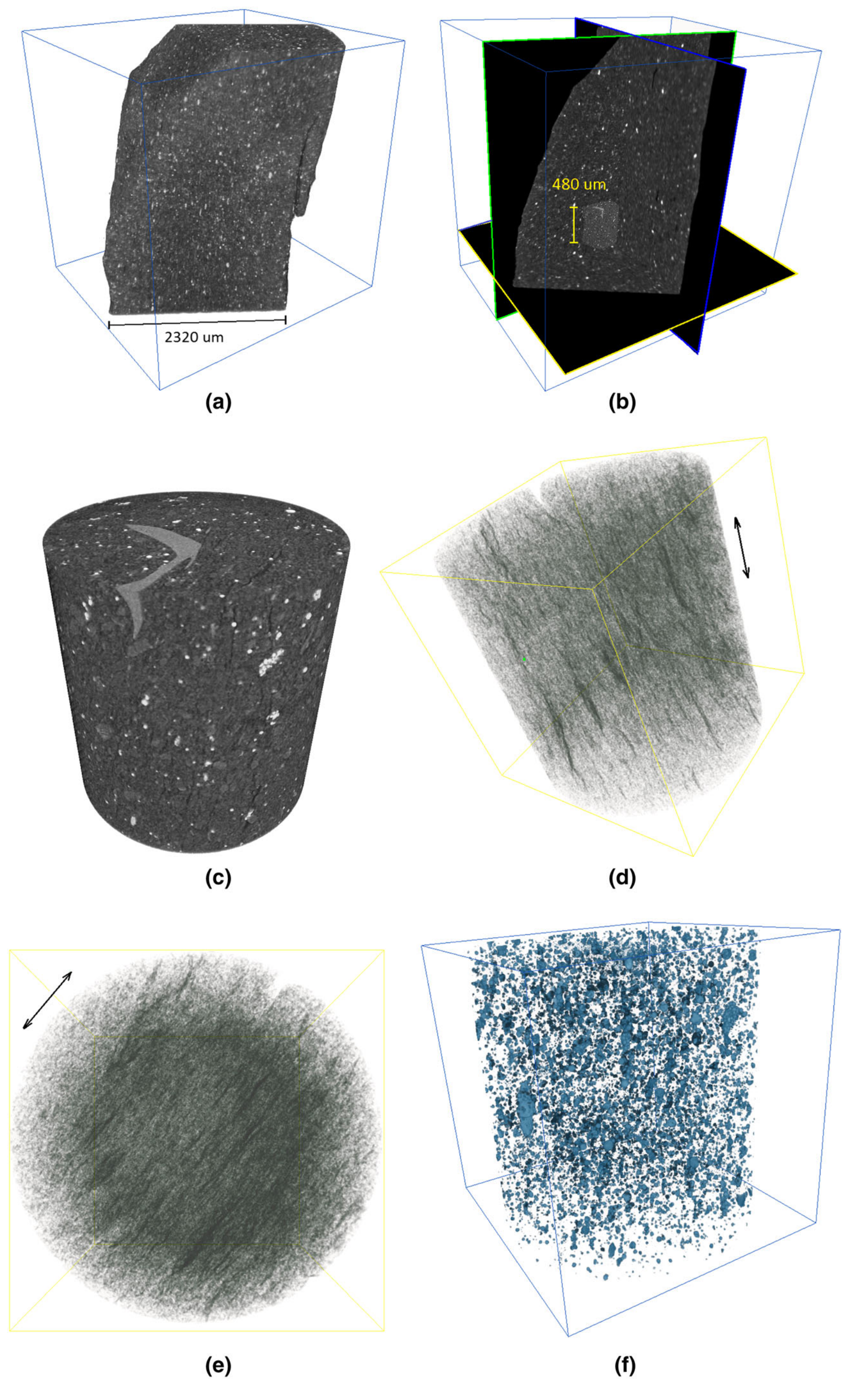

Fig. 3 3D visualization of micro-tomography results. **a** 3D visualization of the millimeter-sized sample of Woodford shale imaged using micro-tomography with a pixel size of 4.14 µm. Cylindrical portion of the sample scanned with pixel size of 0.517 µm is shown in (**b**, **c**). Height of the cylinder is 480 µm and its diameter is 463 µm. **d**, **e** Show cracks and pores inside the high-resolution volume, demonstrating strong anisotropy. *Arrows* on (**d**, **e**) show bedding plane directions. Pyrite particles are segmented as shown in (**f**), which take about 10% of the volume. Images were processed and visualized using ORS Visual SI Advanced

the low-resolution dataset, and Fig. 3c provides the enlarged view of the high-resolution volume. Segmentation of the high-resolution volume into fractures and pores (Fig. 3d, e), as well as pyrite (Fig. 3f), is also shown. Figure 3d, e demonstrates anisotropy in the form of preferred orientation of cracks and pores. To facilitate high-resolution simulations, we selected the ratio between pixel sizes of the low-resolution and high-resolution scans to be an integer by adjusting the source and detector distance in the micro-CT instrument, which determines the pixel size. This is not a necessary condition, however, and in general, the conditioning (low-resolution) secondary data at each pixel in the fine-scale simulation grid can be determined based on the weighted average of the secondary values covering that particular pixel.

4 Results and discussion

For purposes of illustrating the proposed approach, we carry out high-resolution simulations using 2D slices. High-resolution 3D realizations can be similarly generated using 3D tomography data. Figure 4a, b shows, respectively, the selected high- and low-resolution images to be used as a two-variate TI.

Two slices, numbered 1 and 2, shown in Fig. 4c, are selected for simulation using their corresponding low-resolution images given in Figs. 5a and 7a. In this case, each pixel in a low-resolution image contains 64 high-resolution pixels. The simulations were conducted using the program "DS: Multiple-Points Simulation by Direct Sampling" [41]. Appropriate parameters used in DS simulations need to be determined for the specific problem at hand. An extensive guide for parameter selection for DS algorithm is provided in [42]. For the examples presented here various parameters were tested and the following were found to be suitable: $t = 0.01$ and $w_l = w_h = 0.5$ as defined in Eq. (4); and maximum fraction of TI scanned, $F = 1$. Manhattan distance has been used in all the simulations to calculate the distance in Eq. (4). Also, maximum number of neighboring

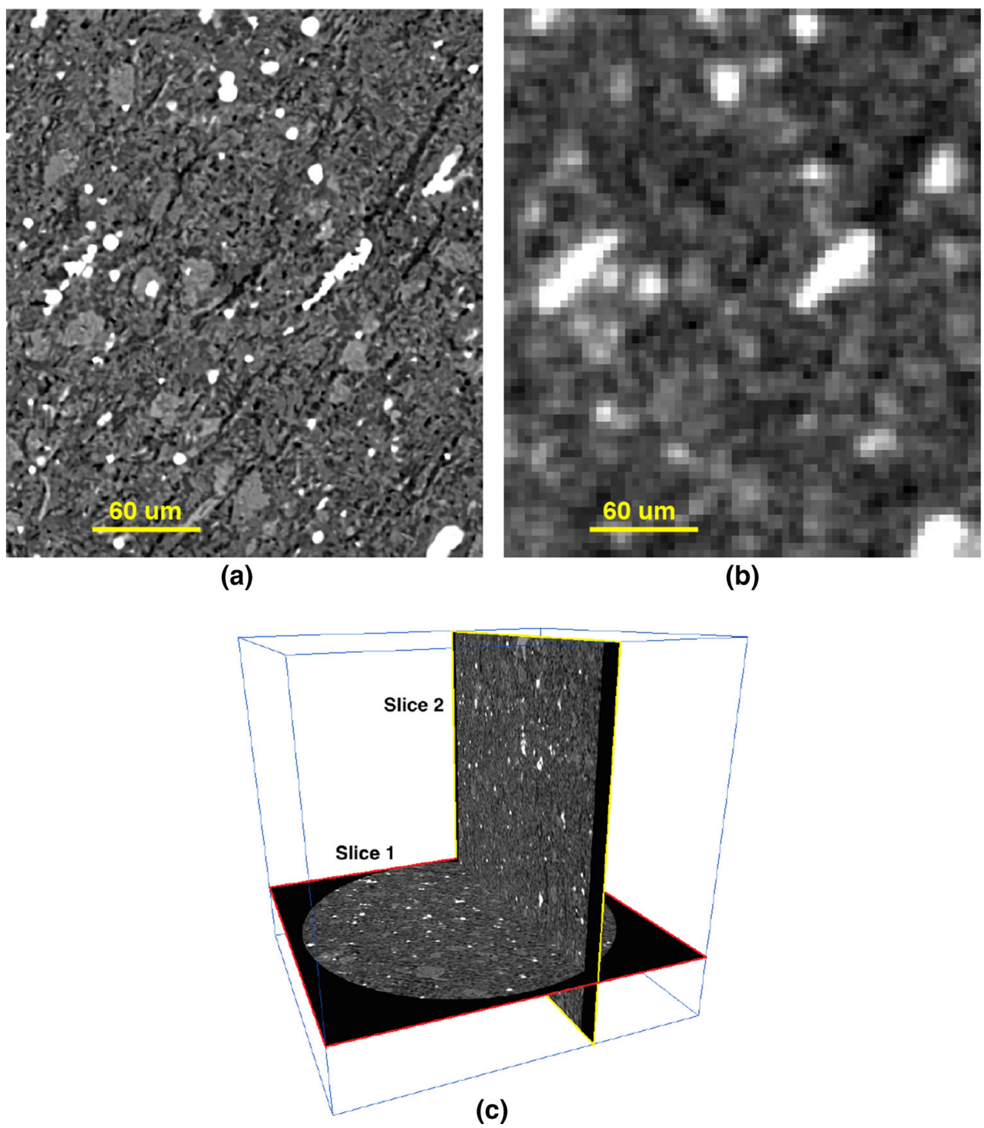

Fig. 4 **a** 2D slice obtained from the high-resolution scan and **b** the corresponding region obtained from the low-resolution scan form the two-variate training image used for the present simulations. The two slices shown in (**c**) are selected to be simulated using only their corresponding low-resolution image as conditioning data

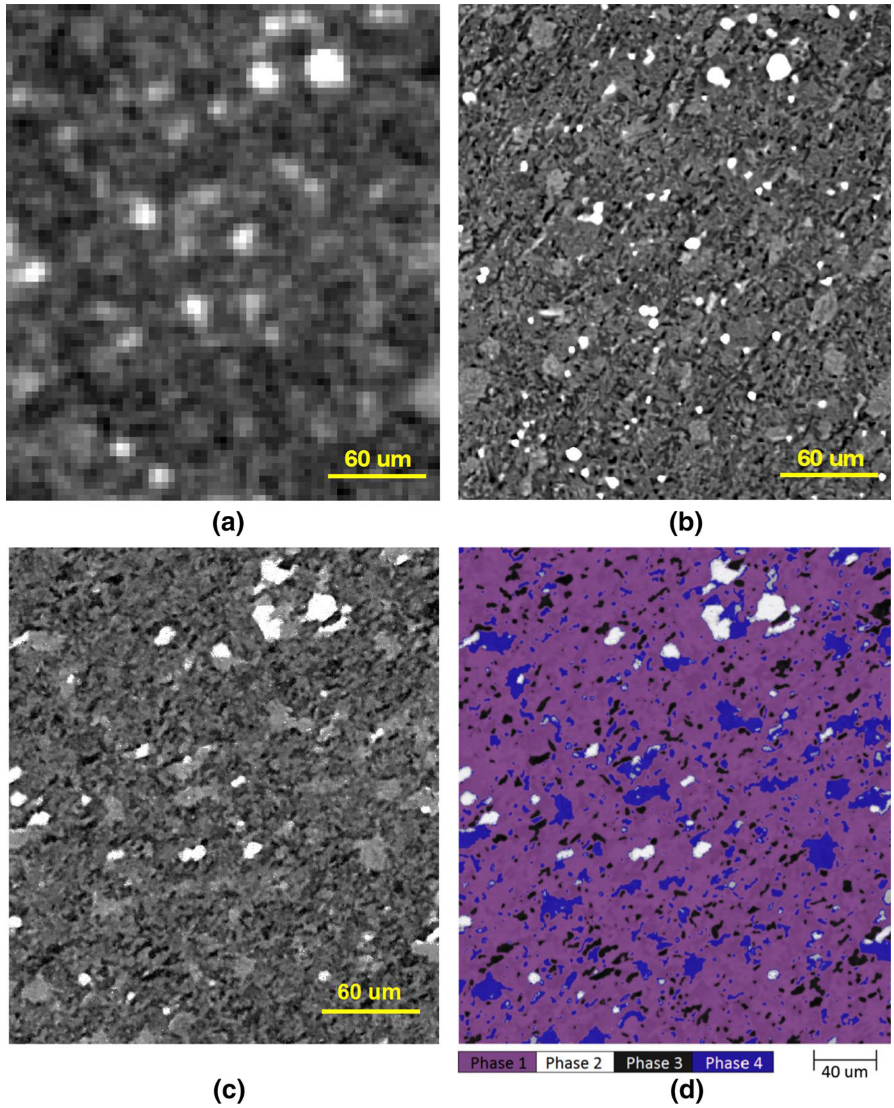

Fig. 5 **a** Low-resolution image corresponding to Slice 1 shown in Fig. 4c, used for high-resolution simulations. **b** True high-resolution image of Slice 1. **c** One realization obtained using the present approach. **d** Segmentation of the realization shown in (**c**) into four phases

pixels used to determine data events defined in Eqs. (2) and (3) was set to 40 over a maximum search distance of 20 pixels in each direction.

Figures 5c and 7c each show a single realization of Slice 1 and Slice 2, respectively. In the present work, we use three different ways to compare each simulated image with its corresponding true image: variogram, pixel-wise error histogram, and visual comparison.

Variogram serves as a measure of spatial continuity of the data and is defined as follows [35]:

$$\gamma(\boldsymbol{h}) = \frac{1}{2} E\left[(Z_h(\boldsymbol{x}) - Z_h(\boldsymbol{x} + \boldsymbol{h}))^2 \right] \tag{5}$$

where $\boldsymbol{h}$ is the lag distance. Figures 6a–c and 8a–c compare variograms of the realizations and true images in horizontal, vertical, and diagonal (from lower left to upper right corner of the image) directions. It can be seen from these plots that the simulated images capture the spatial continuity of the true image in various directions. True images shown in Figs. 5b and 7b are used to obtain the pixel-wise error between each true image and the corresponding simulated field. The histograms of normalized errors are plotted in Figs. 6d and 8d, with mean μ, standard deviation σ and skewness δ shown on each plot. It can be seen that the mean of errors is zero and standard deviation is relatively small ($\sigma = 0.16$) for both images, showing that a majority of the simulated pixels are close to the true value.

By visual comparison, we observe that Fig. 5b has a relatively isotropic structure with a slight preferential orientation of microcracks and pores in the diagonal direction, and simulated image in Fig. 5c captures the same pattern. On the other hand, Fig. 7b demonstrates cracks and

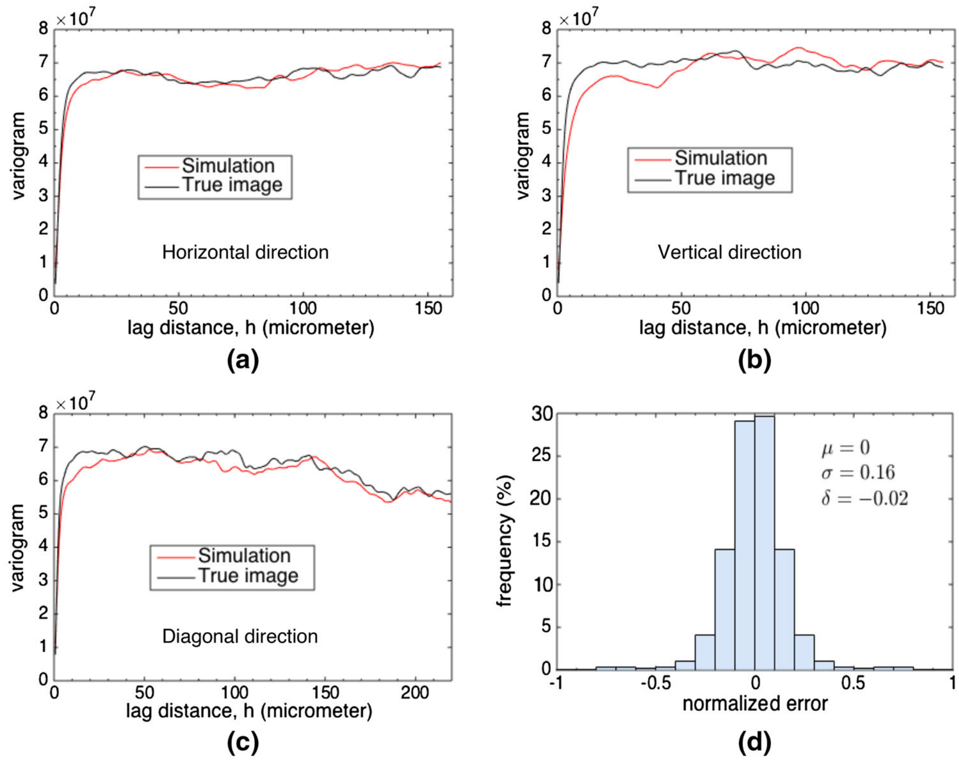

Fig. 6 **a**, **b**, **c** Comparison of variograms of the simulation result with the true image in horizontal, vertical, and diagonal (*lower left* to *upper right corner* of the image) directions. **d** Histogram of pixel-wise normalized error between Figs. 5b and 5c

particles along the vertical direction, which can also be observed in the simulated Fig. 7c.

It should be noted that here we have chosen to work with continuous variables, i.e., gray values, as opposed to categorical variables (i.e., individual phases). This scheme provides two main advantages. First, as described earlier, low-resolution images provide information about features below their resolution limit which cannot be segmented into individual phases. Therefore, using continuous variables for low-resolution data allows us to readily condition the simulations on these data. Second, high-resolution images are simulated pixel by pixel, which may lead to generation of a number of "noisy" pixels not fully consistent with their neighbors. Application of continuous variables for high-resolution simulations facilitates subsequent filtering and denoising. Statistically simulated images can be treated as high-resolution X-ray tomography data. Therefore, post-simulation processing needs to be done on the simulated images, which mainly consists of the following:

1. Application of denoising and filtering algorithms, e.g., bm4d [38], non-local means [16], or smoothing using kriging [39].
2. Well-known image segmentation techniques can be used to segment the simulated grayscale images into different phases [48].

The realizations shown in Figs. 5c and 7c are filtered and segmented into four phases as follows. Phase 1: mixture of clay, organics, and minerals matrix; Phase 2: high-density minerals (e.g., pyrite); Phase 3: fractures and pores; Phase 4: light minerals (e.g., silicates). The segmentations are performed based on histogram thresholding, and the segmented images are shown in Figs. 5d and 7d. Figure 9 shows the comparison of the phase proportions of the simulated images with those of the true images, obtained using the same histogram thresholding criteria. It should be noted that this shale sample contains features below the 0.7 μm resolution limit of the micro-CT instrument (e.g., nano-pores, organic matter, and submicron particles shown in Fig. 1g) which are not resolved. Therefore, the segmentation is performed here to compare the true images and their corresponding simulated images, rather than reporting the exact proportions of individual phases. Figure 9 shows that the phase proportions in the segmented simulated images are consistent with those of the true images segmented using the same criteria. This is important, for example, in flow simulations where porosity of the sample is one of the important factors that need to be captured.

It is worth noting that scan parameters such as X-ray energy affect X-ray attenuations of different material phases, which would result in differences in the grayscale images obtained with different settings. Since the high-

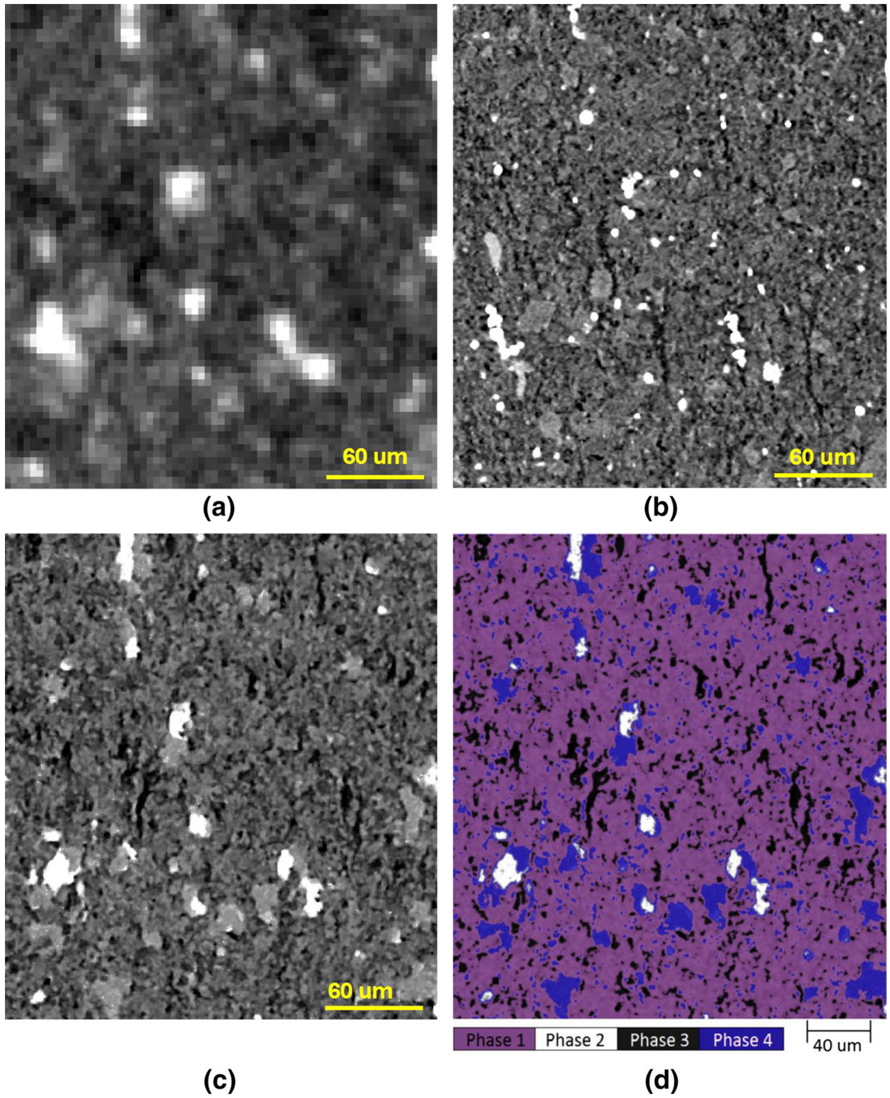

Fig. 7 **a** Low-resolution image corresponding to Slice 2 shown in Fig. 4c, used for high-resolution simulations. **b** True high-resolution image of Slice 2. **c** One realization obtained using the present approach. **d** Segmentation of the realization shown in (**c**) into four phases

resolution and low-resolution scans typically require different scan parameters, it is normally expected that the gray values in the large-FOV and high-resolution scans from the same region would not be directly comparable. This does not pose any problems, since according to the nature of the described algorithm, the low-resolution images and their corresponding high-resolution images do not need to be comparable in terms of the gray values, as they are two separate variables. The low-resolution and high-resolution variables from the simulation domain are compared separately with their corresponding values in the training image in order to calculate the distance define in Eq. (4). However, it is essential for the grayscale low-resolution images in the TI and the simulation field to be comparable. In the present work, the low-resolution images were selected from a single large-FOV scan and were subjected to the same image processing. In general, to assure consistency between low-resolution images in the TI and the simulation field, a uniform histogram transformation with support parameters of 0 and 1 can be done for all the images. After performing the simulations, the histogram of images must then be transformed back to the histogram of TI or another suitable image.

5 Concluding remarks

We have demonstrated an approach based on MPS to generate high-resolution images of shale conditioned on the observed low-resolution images. Simulation results were shown to be consistent with the true images obtained from high-resolution scans, which suggests that this

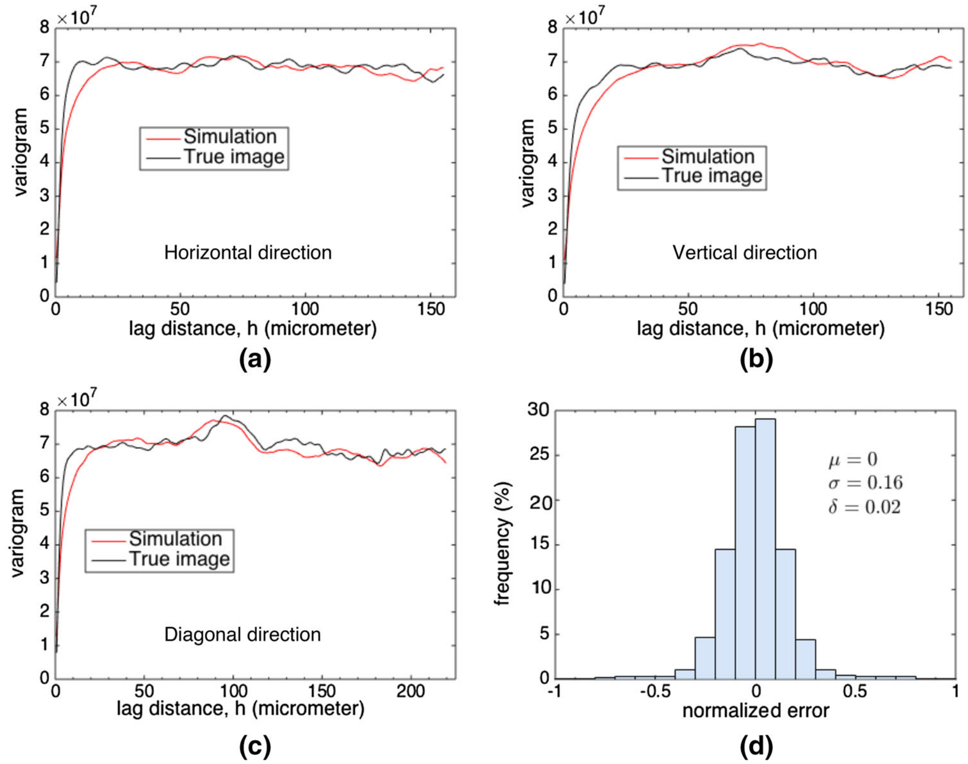

Fig. 8 **a**, **b**, **c** Comparison of variograms of the simulation result with the true imagein horizontal, vertical, and diagonal (*lower left* to *upper right corner* of the image) directions. **d** Histogram of pixel-wise normalized error between Figs. 7b and 7c

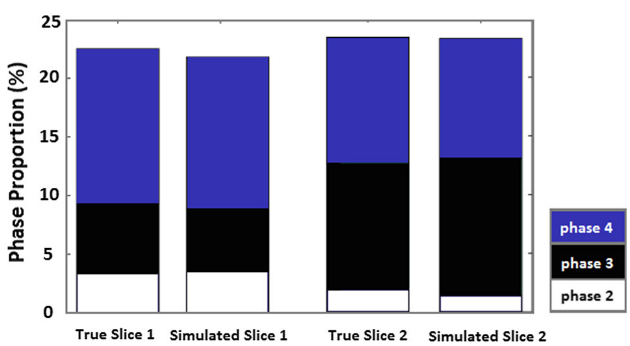

Fig. 9 Comparison of the phase proportions between the true high-resolution images and the simulation results

approach can offer a solution to the trade-off between imaging resolution and FOV associated with imaging of heterogeneous materials. The results here were shown for 2D simulations, but the same procedure applies to 3D simulations.

It is worth emphasizing that the present approach is statistical in nature and that it is not meant to generate an image that exactly matches the true field. Instead, the goal is to generate high-resolution realizations of the field that are consistent with the observed low-resolution images and are similar to the true field in terms of structural features such as patterns, connectivity, anisotropy, and histogram. There is generally no practical limitation on the ratio of pixel sizes in the low-resolution and high-resolution images. As an extreme example, if the whole high-resolution image corresponds to one or a few low-resolution pixels, the low-resolution image in this case does not provide any useful information and there will practically be no conditioning on the low-resolution data. In this case, the algorithm will randomly generate a microstructure based on patterns obtained from the high-resolution training image, similar to having a univariate TI. Clearly, the more information the low-resolution image has, and/or the closer the pixel sizes are to the fine-scale field, the more accurate the simulations. Therefore, the sufficient pixel sizes for the high-resolution and low-resolution data in order to provide meaningful patterns within both datasets need to be determined for the specific material being studied. Additionally, it is important for a TI to include the patterns expected in the simulation field.

Finally, we note that the proposed multiscale imaging approach has vast applications to computational modeling as well. An example is mesh sensitivity study in finite element analysis, which is a routine task when the domain of the problem is spatially homogeneous. However, when the domain of the problem is characterized by spatially varying material properties, such as density and degree of saturation [14, 15, 52, 53], then the refinement in the mesh must be accompanied by the corresponding refinement in the spatial description of material heterogeneity. Note that a mesh sensitivity study does not necessarily require the true high-resolution field but only a high-resolution realization of the field that is consistent with the coarse mesh, so the proposed statistical approach may be used for this purpose. Multiscale finite element analyses requiring detailed microstructure characterization at the Gauss integration points [8, 28, 46] may also benefit from the proposed MPS approach, particularly when the true high-resolution field is not available over the entire problem domain.

Acknowledgements This material is based upon work supported by the U.S. Department of Energy, Office of Science, Office of Basic Energy Sciences, Geosciences Research Program, under Award No. DE-FG02-03ER15454. Support for materials and additional student hours were provided by the National Science Foundation under Award No. CMMI-1462231. We acknowledge the use of Stanford Nano Shared Facilities (SNSF), which is supported by the National Science Foundation under Award ECCS-1542152, at Stanford University for X-ray micro-tomography imaging, and thank Dr. Arturas Vailionis of SNSF for training and support in conducting the experimental portion of the work. We also thank Dr. Younane N. Abousleiman of the University of Oklahoma for providing samples of Woodford shale, and Dr. Grégoire Mariethoz of University of Lausanne for providing the program "DS: Multiple-Points Simulation by Direct Sampling". The first author acknowledges the National Science Foundation for a Graduate Research Fellowship under Grant No. DGE-114747.

References

1. Abedi S, Slim M, Ulm F-J (2016) Nanomechanics of organic-rich shales: the role of thermal maturity and organic matter content on texture. Acta Geotech 11(4):775–787
2. Abedi S, Slim M, Hofmann R, Bryndzia T, Ulm F-J (2016) Nanochemo-mechanical signature of organic-rich shales: a coupled indentation-EDX analysis. Acta Geotech 11(3):559–572
3. Abousleiman Y, Tran M, Hoang S, Bobko C, Ortega A, Ulm F-J (2007) Geomechanics Field and Laboratory Characterization of Woodford Shale: The Next Gas Play. In: Proceedings–SPE Annual Technical Conference and Exhibition held in Anaheim. California, USA, pp 2127–2140
4. Abousleiman YN, Hull KL, Han Y, Al-Muntasheri G, Hosemann P, Parker S, Howard CB (2016) The granular and polymer composite nature of Kerogen-rich shale. Acta Geotech 11(3):573–594
5. Adler PM, Jacquin CG, Quiblier JA (1990) Flow in simulated porous media. Int J Multiph Flow 16(4):691–712
6. Alikarami R, Andò E, Gkiousas-Kapnisis M, Torabi A, Viggiani G (2015) Strain localisation and grain breakage in sand under shearing at high mean stress: insights from in situ X-ray tomography. Acta Geotech 10:15–30
7. Almarzooq A, AlGhamdi T, Koronfol S, Dernaika M, Walls J (2014) Shale gas characterization and property determination by digital rock physics. In: Paper SPE-172840-MS presented at the SPE-SAS Annual Technical Symposium and Exhibition, Al Khobar, Saudi Arabia, 21–24 April
8. Andrade JE, Avila CF, Hall SA, Lenoir N, Viggiani G (2011) Multiscale modeling and characterization of granular matter: from grain kinematics to continuum mechanics. J Mech Phys Solids 59(2):237–250
9. Arns CH, Bauget F, Limaye A, Sakellariou A, Senden TJ, Sheppard AP, Sok RM, Pinczewski WV, Bakke S, Berge LI, Øren P-E (2005) Pore scale characterization of carbonates using X-ray microtomography. SPE J 10(4):475–484
10. Bennett KC, Berla LA, Nix WD, Borja RI (2015) Instrumented nanoindentation and 3D mechanistic modeling of a shale at multiple scales. Acta Geotech 10:1–14
11. Borja RI, Choo J (2016) Cam-Clay plasticity, Part VIII: a constitutive framework for porous materials with evolving internal structure. Comput Methods Appl Mech Eng 309:653–679
12. Borja RI, Rahmani H (2012) Computational aspects of elasto-plastic deformation in polycrystalline solids. J Appl Mech 79(3):031024
13. Borja RI, Rahmani H (2014) Discrete micromechanics of elastoplastic crystals in the finite deformation range. Comput Methods Appl Mech Eng 275:234–263
14. Borja RI, Song X, Rechenmacher AL, Abedi S, Wu W (2013) Shear band in sand with spatially varying density. J Mech Phys Solids 61(1):219–234
15. Borja RI, Andrade JE (2006) Critical state plasticity. Part VI: meso-scale finite element simulation of strain localization in discrete granular materials. Comput Methods Appl Mech Eng 195(37–40):5115–5140
16. Buades A, Coll B, Morel JM (2005) A non-local algorithm for image denoising. In: Proceedings of the IEEE Computer Society Conference on Computer Vision and Pattern Recognition, vol 2, pp 60–65
17. Čapek P, Hejtmánek V, Brabec L, Zikánová A, Kočiřík M (2009) Stochastic reconstruction of particulate media using simulated annealing: improving pore connectivity. Transp Porous Media 76(2):179–198
18. Cnudde V, Boone MN (2013) High-resolution X-ray computed tomography in geosciences: a review of the current technology and applications. Earth Sci Rev 123:1–17
19. Curtis ME, Sondergeld CH, Ambrose RJ, Rai CS (2012) Microstructural investigation of gas shales in two and three dimensions using nanometer-scale resolution imaging. AAPG Bull 96(4):665–677
20. Desbois G, Urai JL, Hemes S, Schröppel B, Schwarz J-O, Mac M, Weiel D (2016) Multi-scale analysis of porosity in diagenetically altered reservoir sandstone from the Permian Rotliegend (Germany). J Petrol Sci Eng 140:128–148
21. Druckrey AM, Alshibli KA (2016) 3D finite element modeling of sand particle fracture based on in situ X-ray synchrotron imaging. Int J Numer Anal Meth Geomech 40(1):105–116
22. Efros AA, Freeman WT (2001) Image quilting for texture synthesis and transfer. In: Proceedings of the 28th Annual Conference on Computer Graphics and Interactive Techniques (ACM, 2001), pp 341–346
23. Epting WK, Gelb J, Litster S (2012) Resolving the three-dimensional microstructure of polymer electrolyte fuel cell electrodes using nanometer-scale X-ray computed tomography. Adv Funct Mater 22(3):555–560
24. Feyen L, Caers J (2006) Quantifying geological uncertainty for flow and transport modeling in multi-modal heterogeneous formations. Adv Water Resour 29(6):912–929
25. Gelb J, Gu A, Fong T, Hunter L, Lau SH, Yun W (2011) A closer look at shale: representative elementary volume analysis with laboratory 3D X-ray computed microtomography and nanotomography. In: Paper SCA2011-58 presented at the international symposium of the society of core analysts held in Austin, Texas, USA, 18–21 September

26. Gerke KM, Karsanina MV, Mallants D (2015) Universal stochastic multiscale image fusion: an example application for shale rock. Sci Rep 5:15880
27. Grader AS, Clark ABS, Al-Dayyani T, Nur A (2009) Computations of porosity and permeability of sparic carbonate using multi-scale CT images. In: 23rd international symposium of the society of core analysts, Noordwijk aan Zee, Netherlands, 27–30 September
28. Guo N, Zhao J (2016) Multiscale insights into classical geomechanics problems. Int J Numer Anal Meth Geomech 40(3):367–390
29. Hemes S, Desbois G, Urai JL, Schröppel B, Schwarz J-O (2015) Multi-scale characterization of porosity in Boom Clay (HADES-level, Mol, Belgium) using a combination of X-ray μ-CT, 2D BIB-SEM and FIB-SEM tomography. Microporous Mesoporous Mater 208:1–20
30. Hu LY, Chugunova T (2008) Multiple-point geostatistics for modeling subsurface heterogeneity: a comprehensive review. Water Resour Res 44(11):W11413
31. Jha SK, Mariethoz G, Evans JP, McCabe MF (2013) Demonstration of a geostatistical approach to physically consistent downscaling of climate modeling simulations. Water Resour Res 49(1):245–259
32. Josh M, Esteban L, Delle Piane C, Sarout J, Dewhurst DN, Clennell MB (2012) Laboratory characterization of shale properties. J Petrol Sci Eng 88:107–124
33. Keller LM, Schuetz P, Erni R, Rossell MD, Lucas F, Gasser P, Holzer L (2013) Characterization of multi-scale microstructural features in Opalinus Clay. Microporous Mesoporous Mater 170:83–94
34. Khalili AD, Arns CH, Arns JY, Hussain F, Cinar Y, Pinczewski WV, Latham S, Funk J (2012) Permeability upscaling for carbonates from the pore-scale using multi-scale X-ray-CT images. In: Paper SPE 152640 presented in SPE/EAGE European Unconventional Resources Conference and Exhibition, Vienna, Austria, 20–22 March
35. Krishnan S, Journel AG (2003) Spatial connectivity: from variograms to multiple-point measures. Math Geol 35(8):915–925
36. Lemmens H, Richards D (2013) Multiscale imaging of shale samples in the scanning electron microscope. In: Camp W, Diaz E, Wawak B (eds) Electron Microscopy of Shale Hydrocarbon Reservoirs, 102. AAPG Memoir, Tulsa, pp 27–35
37. Lenoir N, Bornert M, Desrues J, Bésuelle P, Viggiani G (2007) Volumetric digital image correlation applied to X-ray microtomography images from triaxial compression tests on argillaceous rock. Strain 43(3):193–205
38. Maggioni M, Katkovnik V, Egiazarian K, Foi A (2013) Nonlocal transform-domain filter for volumetric data denoising and reconstruction. IEEE Trans Image Process 22(1):119–133
39. Mahmud K, Mariethoz G, Baker A, Sharma A (2015) Integrating multiple scales of hydraulic conductivity measurements in training image-based stochastic models. Water Resour Res 51(1):465–480
40. Manwart C, Torquato S, Hilfer R (2000) Stochastic reconstruction of sandstones. Phys Rev E 62(1):893–899
41. Mariethoz G, Renard P, Straubhaar J (2010) The direct sampling method to perform multiple-point geostatistical simulations. Water Resour Res. doi:10.1029/2008WR007621
42. Meerschman E, Pirot G, Mariethoz G, Straubhaar J, Van Meirvenne M, Renard P (2013) A practical guide to performing multiple-point statistical simulations with the direct sampling algorithm. Comput Geosci 52:307–324
43. Mehrabian A, Abousleiman YN (2015) Gassmann equations and the constitutive relations for multiple-porosity and multiple-permeability poroelasticity with applications to oil and gas shale. Int J Numer Anal Meth Geomech 39(14):1547–1569
44. Meirer F, Cabana J, Liu Y, Mehta A, Andrews JC, Pianetta P (2011) Three-dimensional imaging of chemical phase transformations at the nanoscale with full-field transmission X-ray microscopy. J Synchrotron Radiat 18(5):773–781
45. Mustapha H, Dimitrakopoulos R (2010) A new approach for geological pattern recognition using high-order spatial cumulants. Comput Geosci 36(3):313–334
46. Nguyen TK, Combe G, Caillerie D, Desrues J (2014) FEM $\times$ -DEM modelling of cohesive granular materials: numerical homogenisation and multi-scale simulations. Acta Geophys 62(5):1109–1126
47. Okabe H, Blunt MJ (2005) Pore space reconstruction using multiple-point statistics. J Petrol Sci Eng 46(1):121–137
48. Schlüter S, Sheppard A, Brown K, Wildenschild D (2014) Image processing of multiphase images obtained via X-ray microtomography: a review. Water Resour Res 50(4):3615–3639
49. Semnani SJ, White JA, Borja RI (2016) Thermo-plasticity and strain localization in transversely isotropic materials based on anisotropic critical state plasticity. Int J Numer Anal Methods Geomech 40(18):2423–2449
50. Soares A (2001) Direct sequential simulation and cosimulation. Math Geol 33(8):911–926
51. Sok RM, Knackstedt MA, Varslot T, Ghous A, Latham S, Sheppard AP (2010) Pore scale characterization of carbonates at multiple scales: integration of micro-CT, BSEM, and FIBSEM. Petrophysics 51(6):379–387
52. Song X, Borja RI (2014) Mathematical framework for unsaturated flow in the finite deformation range. Int J Numer Methods Eng 97(9):658–682
53. Song X, Borja RI (2014) Finite deformation and fluid flow in unsaturated soils with random heterogeneity. Vadose Zone J. doi:10.2136/vzj2013.07.0131
54. Strebelle S (2002) Conditional simulation of complex geological structures using multiple-point statistics. Math Geol 34(1):1–21
55. Tatone BSA, Grasselli G (2015) Characterization of the effect of normal load on the discontinuity morphology in direct shear specimens using X-ray micro-CT. Acta Geotech 10:31–54
56. Tjioe M, Borja RI (2015) On the pore-scale mechanisms leading to brittle and ductile deformation behavior of crystalline rocks. Int J Numer Anal Methods Geomech 39:1165–1187
57. Tjioe M, Borja RI (2016) Pore-scale modeling of deformation and shear band bifurcation in porous crystalline rocks. Int J Numer Methods Eng 108:183–212
58. Vega B, Andrews JC, Liu Y, Gelb J, Kovscek A (2013) Nanoscale visualization of gas shale pore and textural features. In: Paper 1581981 presented at the Unconventional Resources Technology Conference. Denver, Colorado, 12–14 August
59. Verde A, Ghassemi A (2016) Large-scale poroelastic fractured reservoirs modeling using the fast multipole displacement discontinuity method. Int J Numer Anal Methods Geomech 40(6):865–886
60. Walls JD, Diaz E, Cavanaugh T (2012) Shale reservoir properties from digital rock physics. In: Paper SPE 152752 presented at the SPE/EAGE European Unconventional Resources Conference and Exhibition, Vienna, Austria, 20–22 March
61. Wang FP, Reed RM (2009) Pore networks and fluid flow in gas shales. In: Paper SPE-124253-MS presented at the 2009 SPE Annual Technical Conference and Exhibition, New Orleans, LA, 4–7 October
62. Wildenschild D, Sheppard AP (2013) X-ray imaging and analysis techniques for quantifying pore-scale structure and processes in subsurface porous medium systems. Adv Water Resour 51:217–246
63. Wu K, Van Dijke MIJ, Couples GD, Jiang Z, Ma J, Sorbie KS, Crawford J, Young I, Zhang X (2006) 3D stochastic modelling of heterogeneous porous media-applications to reservoir rocks. Transp Porous Media 65(3):443–467

64. Zhang T, Du Y, Huang T, Li X (2015) Reconstruction of porous media using multiple-point statistics with data conditioning. Stoch Environ Res Risk Assess 29(3):727–738
65. Zhang T, Lu D, Li D (2009) Porous media reconstruction using a cross-section image and multiple-point geostatistics. In: International Conference on Advanced Computer Control (IEEE, 2009), pp 24–29
66. Zhou B, Wang J (2017) Generation of a realistic 3D sand assembly using X-ray micro-computed tomography and spherical harmonic-based principal component analysis. Int J Numer Anal Methods Geomech 41:93–109